

On a workflow for efficient computation of the permeability of tight sandstones

Received: date / Accepted: date

This work was supported by the Ministry of Science and Higher Education of the Russian Federation under agreement No. 075-10-2020-119 within the framework of the development program for a world-class Research Center.

V. Pimanov
Skolkovo Institute of Science and Technology, Bolshoy Boulevard 30, bld. 1, Moscow, Russia,
121205
E-mail: Vladislav.Pimanov@skoltech.ru

V. Lukoshkin
Skolkovo Institute of Science and Technology

P. Toktaliev
Fraunhofer Institute for Industrial Mathematics

O. Iliev
Fraunhofer Institute for Industrial Mathematics

E. Muravleva
Skolkovo Institute of Science and Technology

D. Orlov
Skolkovo Institute of Science and Technology

V. Krutko
Gazpromneft Science and Technology Center

A. Avdonin
Gazpromneft Science and Technology Center

K. Steiner
Fraunhofer Institute for Industrial Mathematics

D. Koroteev
Skolkovo Institute of Science and Technology

Contents

1	Introduction.	3
1.1	Motivation and goals.	3
1.2	Contributions.	4
2	Problem statement.	5
2.1	Computational domain.	5
2.2	Governing equations.	6
2.3	Boundary conditions.	7
2.4	Computing effective permeability.	8
3	Numerical method.	9
3.1	Discretization.	9
3.2	Implementations details.	10
4	Preprocessing stage.	11
4.1	Multiclass model preparation.	11
4.2	Sample classification.	12
5	Computational experiments.	12
5.1	Design of computational experiments.	12
5.2	Stokes solver. Validation and performance studies on binary images.	12
5.3	Stokes-Brinkman and Darcy solvers. Validation and performance studies on ternary and multiclass images from tight reservoir rocks.	14
5.3.1	Preliminaries: Goals and samples.	14
5.3.2	Simulations on ternary images of size 300^3	16
5.3.3	Simulations on multiclass image of size 300^3	18
5.3.4	Simulations on ternary images of size 600^3 and 1350^3	19
5.4	Summary.	20
A	Simulations on S1 ternary images of size 300^3	23
B	Darcy approximation, sensitivity study	24
C	Visual comparison of flow simulations with Stokes-Brinkman system and with its Darcy approximation	25
D	Hardware/Software Specifications	25
E	Simulations on ternary images of size 600^3 and 1350^3	25

Abstract The paper presents a workflow for fast pore-scale simulation of single-phase flow in tight reservoirs typically characterized by low, multiscale porosity. Multiscale porosity implies that the computational domain contains porous voxels (unresolved porosity) in addition to pure fluid voxels. In this case, the Stokes-Brinkman equations govern the flow, with the Darcy term needed to account for the flow in the porous voxels. As the central part of our workflow, robust and efficient solvers for Stokes and Stokes-Brinkman equations are presented. The solvers are customized for low-porosity binary and multiclass images, respectively. Another essential component of the workflow is a preprocessing module for classifying images with respect to the connectivity of the multiscale pore space. Particularly, an approximation of the Stokes-Brinkman problem, namely, the Darcy problem, is investigated for the images that do not have pure fluid percolation paths. Thorough computational experiments demonstrate efficiency and robustness of the workflow for simulations on images from tight reservoirs. Raw files describing the used CT images are provided as supplementary materials to enable other researchers to use them.

Keywords Pore-scale flow simulation · Tight reservoirs · Multi-scale porosity · Stokes-Brinkman equations · Stokes equations · Darcy equations · Robust preconditioning

1 Introduction.

1.1 Motivation and goals.

Today the leading oil companies of the global energy perspective put forth great efforts to have commercial and stable production from tight and ultra-tight hydrocarbon resources in which the initial reserves are enormously more significant than the reserve of conventional resources. Despite all technological achievements, the development of unconventional resources might yet be a risky investment if it is not supported well with detailed and accurate reservoir studies [46]. As a result and subject to the requirements of reservoir studies and relevant challenges, developing techniques, methods, and instruments for the comprehensive evaluation of unconventional hydrocarbon studies is currently an important area of research [26].

Regardless of many attempts that have been made to modify the conventional methods of core analysis suitable to be applied for the evaluation of unconventional hydrocarbon resources [29], they are still time-consuming, expensive, and inaccurate [38]. It is mainly due to the existence of sub-micron pores and throats that have strong effects on the storage and flow of tight and ultra-tight oil and gas resources [9, 18].

To fit the risk attitude of the decision-makers, applying modern methods of core analysis like Digital Rock Physics, DRP, has mainly been focused on over the last decade [22, 21]. Besides the fact that DRP is an efficient cost control and risk management method, it allows the researchers to perform multiple numerical experiments on exactly the same sample and implement various analyses simultaneously [19, 45].

Single-phase flows are attracting significant attention in DRP. A number of commercial [41, 31, 33] and academic [32, 25, 24, 4] flow solvers have been devel-

oped, to name just a few. These and many others are currently actively used for solving scientific, environmental, and industrial problems, as well as in benchmark studies [1, 40]. Despite the active development of algorithms and software in DRP, pore-scale simulations for tight reservoirs, usually characterized by low, multiscale porosity, remain a challenge. It should be noted that not only the tight reservoir rocks are characterized by multiscale porosity. There are also plenty of examples beyond natural rocks, e.g., active carbon particles in nonwoven filtering materials used for air filtration, catalyst in diesel particulate filters for automotive applications, bones, especially in the case of osteoporosis, etc. In such cases, despite the high imaging resolution, there is often unresolved porosity as a part of the image. Cutting-edge research is currently carried out to investigate the impact of the unresolved porosity on the considered problems. Due to the enormous complexity of the pore geometry, the variation of the material properties in the unresolved regions, the jumping coefficients, the large size of the computational domains, the existing numerical algorithms cannot always provide satisfactory results. The flow solvers developed for computing permeability for higher porosity in certain cases fail to converge for images of tight rocks. The demand for developing advanced customized algorithms in this area has risen essentially in the last years.

1.2 Contributions.

The ultimate objective of this paper is to propose a workflow for solving single-phase pore-scale flow problems in tight sandstones characterized by low or very low porosity and connectivity, especially in the case of the appearance of unresolved porosity. The workflow has essentially three components.

- (i) The first stage, as usually, is the image processing. The multiclass models of real rock samples from tight reservoirs considered here are built according to the approach from [3], with the help of the double μ CT scanning technique. The details of the model preparation process is a subject of follow up article, a sketch is briefly described in Section 4.1.
- (ii) At the second stage, the 3D images (multiclass models) are classified with respect to the connectivity of the resolved pore space.
- (iii) At the third stage, either the newly developed Stokes-Brinkman or Darcy solver is used to calculate the effective permeability for different classes of images.

Extensive studies are carried out on the performance of the presented solvers. The simulation results illustrate the high accuracy and robustness of the Stokes-Brinkman solver. Its superior performance in computing permeability for tight rocks is demonstrated in comparison with state-of-the-art Stokes-Brinkman commercial solvers for DRP. The usage of the Darcy approximation of the Stokes-Brinkman equations to compute the permeability of images without pure fluid percolation paths is explored, and it shows a significant reduction of the CPU time, while providing good accuracy. Note that the idea of solving the Darcy problem instead of the Stokes-Brinkman one is not a new one; it was earlier explored, e.g., in [25]. Here this approach is a part of our workflow, which is equipped with a preprocessor module (classifier) to automatically decide if it is reasonable to solve the Darcy approximation.

Although the workflow is primarily intended for multiclass images, the robust Stokes solver for low porosity binary images is presented as well.

The remainder of the paper is organized as follows. Section 2 is devoted to the statement of the boundary value problem for single-phase flow in the case of resolved and unresolved porosity. Section 3 discusses the numerical algorithms and their implementation. Section 4 is dedicated to describing the preprocessing stage in the proposed workflow. Section 5 is the core of the paper, it contains the results of the numerical experiments and their discussion. Data from the literature, when possible, and data from computations with the commercial software tool GeoDict [31] are used for the validation. It starts with Subsection 5.1 elaborating on the design of the computational experiments, describing the goals of the simulations. Subsection 5.2 presents validation results for the Stokes solver on binary images. Subsection 5.3 contains results of a thorough numerical investigation of the performance and accuracy of the developed Stokes-Brinkman and Darcy solvers on ternary and multiclass CT images from tight reservoir rocks. Subsection 5.3.1 describes the collection of images used. In subsection 5.3.2, simulation results for 300^3 ternary samples are presented, and the applicability of the Darcy solver is discussed. Subsection 5.3.3 is dedicated to simulations with a multiclass image when each voxel has individual permeability. Subsection 5.3.4 is similar to subsection 5.3.2 but larger samples of sizes 600^3 and 1350^3 are considered there. Finally, in Subsection 5.4 some conclusions are drawn. Appendix containing a part of the results concludes the article.

2 Problem statement.

2.1 Computational domain.

We represent images by a unit cube domain $\overline{\Omega} = [0, 1]^3$ consisting of three non-overlapping parts:

$$\Omega = \Omega_f^h \cup \Omega_p^h \cup \Omega_s^h, \quad (1)$$

where Ω_f^h is a pure fluid part (resolved porosity), Ω_s^h is a solid part, and Ω_p^h denotes a porous space (unresolved porosity). We suppose that these domains are voxelized 3D CT images, with images of tight sandstone being the main target. Namely, the domain Ω is composed from voxels:

$$\omega_{i,j,k} = [(i-1)h; ih] \times [(j-1)h; jh] \times [(k-1)h; kh], \quad i, j, k = \overline{1, N}, \quad h = 1/N,$$

where N is the number of voxels in each dimension. For each voxel $\omega_{i,j,k}$ we prescribe the porosity $\phi_{i,j,k} \in [0, 100] \subset \mathbb{N}$ which defines the partition (1) as follows:

$$\omega_{i,j,k} \subset \begin{cases} \overline{\Omega}_f^h & \text{if } \phi_{i,j,k} = 0, \\ \overline{\Omega}_p^h & \text{if } \phi_{i,j,k} \in (0, 100), \\ \overline{\Omega}_s^h & \text{if } \phi_{i,j,k} = 100. \end{cases} \quad (2)$$

The solid part Ω_s^h is excluded from computations because no equations are prescribed there, and the computational domain becomes:

$$\Omega^h = \Omega_f^h \cup \Omega_p^h.$$

Note that in (2) different porosity, coming from the grey image, can be considered in each porous voxel. We call such images *multiclass images*. However, for the

sake of simplicity, most simulations are performed for *ternary images* with some constant average porosity prescribed to all porous voxels. Furthermore, *binary images* correspond to the case when all the porosity is resolved, and an image consists only of fluid and solid voxels (i.e., $\Omega^h = \Omega_f^h$).

2.2 Governing equations.

Stokes problem for binary images. In the case when all the pores are resolved, the steady state slow flow of incompressible fluid is governed by the *Stokes equations*:

$$\begin{aligned} -\Delta \mathbf{u} + \nabla p &= \mathbf{0} \text{ in } \Omega^h, \\ -\nabla \cdot \mathbf{u} &= 0 \text{ in } \Omega^h, \\ &+ \text{b.c. on } \partial\Omega^h, \end{aligned} \quad (3)$$

where p is the fluid pressure and \mathbf{u} is the fluid velocity. The boundary conditions on $\partial\Omega^h$ will be discussed in Section 2.3.

Stokes-Brinkman problem for ternary and multiclass images. There are two basic approaches for the numerical flow simulation when porous and free-flow regions co-exist at different scales. The first approach is to use the coupled Stokes-Darcy equations (see, e.g., [2, 49, 30]) which consider of different models in different subdomains coupled via proper interface conditions. In DRP, the other approach, namely the Stokes-Brinkman model, sometimes also called the single domain approach, is valid in both the fluid and porous subregions (see, e.g., [12]). Note that often in the literature, such models are called just Brinkman models or Darcy-Brinkman models. However, *Stokes-Brinkman* term is used here to emphasize that pure fluid voxels exist in the domain. In $\Omega^h = \Omega_p^h \cup \Omega_f^h$ we consider the *Stokes-Brinkman equations*:

$$\begin{aligned} -\Delta \mathbf{u} + \mathbf{K}^{-1} \mathbf{u} + \nabla p &= \mathbf{0} \text{ in } \Omega^h, \quad \mathbf{K}^{-1} \geq 0, \\ -\nabla \cdot \mathbf{u} &= 0 \text{ in } \Omega^h, \\ &+ \text{b.c. on } \partial\Omega^h, \end{aligned} \quad (4)$$

where \mathbf{K}^{-1} is the dimensionless inverse permeability tensor, which is scaled by L^2 where L [m] is a given characteristic (physical) length of a sample. Note that, in the fluid part of the domain Ω_f^h , \mathbf{K}^{-1} becomes zero, and formally, one could recognize Stokes equations (3) in the resolved pores.

Brinkman perturbation of the Stokes-Brinkman problem. In tight reservoirs, one may face the necessity to compute the permeability for images where no pure fluid percolation path exists. In such cases, the flow consequently passes fluid and porous subregions; hence the effective permeability of the image is governed by the resistance of the porous subregions, while the resistance of the fluid subdomain could be neglected. For such samples, the perturbation $\tilde{\mathbf{K}}$ of the permeability tensor \mathbf{K} can be considered by introducing a fictitious permeability value K_{Stokes} in the pure fluid voxels from Ω_f^h . Then, $\tilde{\mathbf{K}}^{-1}$ does not vanish in any of the voxels in

Ω^h , and the *Stokes-Brinkman equations* (4) are thus perturbed to the *Brinkman equations*:

$$\begin{aligned} -\Delta \mathbf{u} + \tilde{\mathbf{K}}^{-1} \mathbf{u} + \nabla p &= \mathbf{0} \text{ in } \Omega^h, & \tilde{\mathbf{K}}^{-1} > 0, \\ -\nabla \cdot \mathbf{u} &= 0 \text{ in } \Omega^h, \\ &+ \text{b.c. on } \partial\Omega^h. \end{aligned} \quad (5)$$

The Brinkman equations (see, e.g., [8]) play an important role for classes of porous media flows, e.g., describing more adequately flows in large porosity domains and allowing to account for no-slip boundary conditions. Here, however, they are not used for a more accurate description of the flow, but they are considered as a perturbation to the Stokes-Brinkman equations (4).

Darcy approximation of the Brinkman problem. The Brinkman problem (5) can be further approximated by neglecting the viscous term, which results in the *Darcy equations*:

$$\begin{aligned} \tilde{\mathbf{K}}^{-1} \mathbf{u} + \nabla p &= \mathbf{0} \text{ in } \Omega^h, & \tilde{\mathbf{K}}^{-1} > 0, \\ -\nabla \cdot \mathbf{u} &= 0 \text{ in } \Omega^h, \\ &+ \text{b.c. on } \partial\Omega^h. \end{aligned} \quad (6)$$

It will be shown in this paper that for a certain class of images, the *Darcy equations* (6) can be solved instead of the *Stokes-Brinkman equations* (4) in order to dramatically reduce the computational time while preserving the accuracy of the effective permeability computations.

2.3 Boundary conditions.

Assume, without loss of generality, that z direction is fixed as *flow direction*, and x, y directions as *tangential directions*. Then, the whole boundary $\partial\Omega^h$ is subdivided as follows:

$$\partial\Omega^h = \Gamma_{\text{in}} \cup \Gamma_{\text{out}} \cup \Gamma_{\text{t}} \cup \Gamma_0,$$

where $\Gamma_{\text{in}} = \{\mathbf{x} \in \partial\Omega^h \mid z = 0\}$ is the inlet boundary, $\Gamma_{\text{out}} = \{\mathbf{x} \in \partial\Omega^h \mid z = 1\}$ is the outlet boundary, $\Gamma_{\text{t}} = \{\mathbf{x} \in \partial\Omega^h \mid x = 0, 1 \text{ or } y = 0, 1\}$ denotes boundaries in the tangential directions, and $\Gamma_0 = \overline{\Omega}_s^h \cap (\overline{\Omega}_f^h \cup \overline{\Omega}_p^h)$ denotes internal boundaries.

The rigorous computation of the permeability tensor according to the homogenization theory is based on using periodic boundary conditions, see, e.g., [43]. In the engineering practice, another formulation is more often used; namely, the velocity is prescribed at the inlet Γ_{in} , and the pressure is prescribed at the outlet Γ_{out} . It was shown in [13] that the results obtained with this velocity/pressure formulation are equivalent to the results obtained with periodic boundary conditions. Furthermore, recently in the engineering literature, one more formulation was introduced, namely, the so-called *pressure drop* boundary condition [14]. In this case,

the following set of boundary conditions for equations (3)-(6) is prescribed:

$$\begin{cases} p = p_{\text{in}} , & \frac{\partial \mathbf{u}}{\partial \mathbf{n}} = \mathbf{0} \text{ on } \Gamma_{\text{in}}, \\ p = p_{\text{out}}, & \frac{\partial \mathbf{u}}{\partial \mathbf{n}} = \mathbf{0} \text{ on } \Gamma_{\text{out}}, \\ \mathbf{u} = \mathbf{0} \text{ on } \Gamma_{\text{t}}, \\ \mathbf{u} = \mathbf{0} \text{ on } \Gamma_0, \end{cases} \quad (7)$$

where $(p_{\text{out}} - p_{\text{in}})$ [Pa] defines the pressure drop.

Two types of boundary conditions in flow direction are implemented in our workflow. First one is the pressure drop formulation (7), and the second one is the periodic formulation.

2.4 Computing effective permeability.

The effective permeability tensor, denoted \mathbf{K}^{eff} , is an intrinsic characteristic of the porous geometry, and it is a functional of the solution \mathbf{u} . Computation of the permeability tensor according to the homogenization theory can be found in [43]. Here, the approach most often used in the engineering literature is considered. Orthotropic (diagonal) permeability tensor is assumed: $\mathbf{K}^{\text{eff}} = \text{diag}(k_{xx}^{\text{eff}}, k_{yy}^{\text{eff}}, k_{zz}^{\text{eff}})$. For a selected flow direction z , and for a given pressure drop, the respective component of the permeability tensor k_{zz}^{eff} [m^2] is determined according to the Darcy's law:

$$k_{zz}^{\text{eff}} = \hat{k}_{zz}^{\text{eff}} L^2 = - \frac{\langle u_z \rangle}{p_{\text{out}} - p_{\text{in}}} L^2, \quad (8)$$

where $\hat{k}_{zz}^{\text{eff}}$ is the corresponding component of the dimensionless permeability tensor, and the Darcy's velocity $\langle u_z \rangle$ is calculated by averaging the respective velocity component over the entire volume of the porous sample [47]:

$$\langle u_z \rangle = |\Omega|^{-1} \int_{\Omega^h} u_z dV. \quad (9)$$

It should be noted that in practice, to calculate effective permeability, the following formula is typically used:

$$k_{zz}^{\text{eff}} = - \frac{1}{p_{\text{out}} - p_{\text{in}}} \frac{Q}{A} L^2, \quad (10)$$

where Q [m^3/s] is the volumetric flow rate, A [m^2] is the cross-sectional area of the sample, and the Darcy velocity approximates the flow:

$$\frac{Q}{A} \approx \langle u_z \rangle. \quad (11)$$

3 Numerical method.

3.1 Discretization.

The discretization of the Stokes (3), (Stokes-)Brinkman (4)-(5), or Darcy (6) equations results in a block system of linear equations of the following form:

$$\begin{bmatrix} A & B^T \\ B & 0 \end{bmatrix} \begin{bmatrix} u_h \\ p_h \end{bmatrix} = \begin{bmatrix} f_h \\ 0 \end{bmatrix}, \quad (12)$$

where:

$$A = \begin{cases} -\Lambda, & \text{for equations (3),} \\ -\Lambda + K^{-1}, & \text{for equations (4)-(5),} \\ K^{-1}, & \text{for equations (6).} \end{cases}$$

Matrices A , B , and B^T are discretisations of the velocity vector Laplacian, the pressure gradient, and the velocity divergence operators, respectively. Matrix K^{-1} denotes the inverse permeability matrix that may have zeros on its diagonal in the Stokes-Brinkman case. The nonzeros in the right-hand side f_h appear due to imposing the Dirichlet boundary conditions on the pressure p (or as a volumetric force in case of periodic boundary conditions).

Iterative method. In the Pressure Schur Complement approach (according to the terminology from [42]), the velocity is eliminated from (12) so that an equivalent problem is obtained:

$$Sp_h = g_h, \quad \text{where } S = BA^{-1}B^T, \quad g_h = BA^{-1}f_h. \quad (13)$$

Once the pressure p_h is computed, the velocity field is reconstructed:

$$u_h = A^{-1}(f_h - B^T p_h).$$

The preconditioned conjugate gradient (PCG) method [44,10] is used to solve equation (13):

$$p_h^{k+1} = p_h^k - \alpha_k \hat{S}^{-1} (Sp_h^k - g_h), \quad (14)$$

where α_k is a parameter of the Krylov subspace method (see e.g. [37], Section 9.2). As a preconditioner \hat{S} , we consider the following approximation of the Schur complement matrix S :

$$\hat{S} = BD^{-1}B^T, \quad D = \text{diag}(A). \quad (15)$$

Two-stage inner-outer iterative process is used to solve (13) to avoid computations with full matrices A^{-1} and S . At each iterative step of the outer iterations given by (14), two inner iterative processes are needed. Firstly, the application of S requires an inversion of the velocity matrix A , and, secondly, the preconditioner \hat{S} (15) needs to be inverted. For both cases, the PCG method with Algebraic Multigrid preconditioner is applied. It is also worth clarifying that for the degenerate Darcy case (6), the preconditioner \hat{S} coincides with S , and the outer iterations, as well as the inner iterations for computing the diagonal inverse A^{-1} , trivially converge in one step.

It is worth emphasizing, that the classical SIMPLE (Semi-Implicit algorithm for Pressure Linked Equations) algorithm [35, 7, 23] relies on the same approximation \hat{S} (15) of the Schur complement S . The connection between SIMPLE and \hat{S} is explained, e.g. in [42] (Section 2.2). Namely, the classical SIMPLE can be considered as Richardson method for solving equation (13) preconditioned with \hat{S} . In conjunction with pore-scale single-phase flow simulation SIMPLE is used, e.g., in [32, 27, 16]. SIMPLE was also used as a smoother in Geometric Multigrid when computing effective permeability of academic and real porous geometries, see [17]. Unlike those papers, here \hat{S} is used as a preconditioner for the Conjugate Gradient method, which is known to converge much faster than Richardson method.

3.2 Implementations details.

The above algorithm is implemented in the framework SCoPeS, which includes modules SCoPeS-S, SCoPeS-SB, and SCoPeS-D for solving Stokes, Stokes-Brinkman, and Darcy problems, respectively. The solver is built on top of the PETSc open-source library [6, 5], which provides a linear algebra backend for the scalable (MPI parallel) solution of partial differential equations, including data structures for sparse matrix computations, a context for Krylov subspace methods (PETSc.KSP module), and a variety of preconditioners (PETSc.PC module). Particularly, the PCG method that is used for inverting S , \hat{S} , and A is implemented within PETSc.KSP.KSPCG routine.

Staggered grid. For discretization, we exploit the classical finite-difference scheme on staggered grids [15]. It is worth mentioning that in DRP, the inverse permeability tensor \mathbf{K}^{-1} ($\tilde{\mathbf{K}}^{-1}$) is a piece-wise constant function of the porosity map $\phi_{i,j,k}$, but the degrees of freedom for the velocity components on staggered grids are located on the voxel faces. Therefore, either porosity or permeability should be averaged over the neighbor voxels (arithmetical mean), and the matrix K^{-1} should be constructed respectively.

Solving with A and \hat{S} . When we solve (13), most of the time is spent on inverting matrices A and \hat{S} at each step of the outer iterations (14). The overall efficiency of the method is determined by the efficiency of the constructed preconditioners for A and \hat{S} . Multigrid methods are proven to work well for elliptic equations. However, the classical Geometric Multigrid method is not easy to apply in the case of complex pore-scale geometry. Another difficulty is related to strongly heterogeneous coefficients relevant for the matrix \hat{S} . The Algebraic Multigrid approach generalizes the principles of Geometric Multigrid method for complex geometries and discontinuous coefficients [36]. We use BoomerAMG [50], which has demonstrated excellent performance in solving DRP problems.

Stopping criteria. Let $rtol_S$, $rtol_A$, and $rtol_{\hat{S}}$ be the tolerances for inverting S , A , and \hat{S} , respectively. The stopping criteria for the PCG iterations is determined by the relative residual in unpreconditioned norm (PETSC.KSP.NORM.UNPRECONDITIONED). For example, the outer PCG iterative process (14) stops as soon as:

$$\frac{\|Sp_h^* - g_h\|_2}{\|g_h\|_2} \leq rtol_S. \quad (16)$$

Given $rtol_S$ as an input of the algorithm, we determine $rtol_A$, and $rtol_{\hat{S}}$ as follows:

$$rtol_A = 10^{-2} \cdot rtol_S, \quad rtol_{\hat{S}} = rtol_S.$$

4 Preprocessing stage.

4.1 Multiclass model preparation.

Digital Rock Physics emerged recently as the alternative to conventional laboratory experiments on core samples. For tight reservoir rocks, the usage of DRP is not as straight forward as for higher porosity sandstones. This is due to the inherent trade-off between the spatial resolution of data and the representativeness of the size of the model. For this regime, we developed a new approach to consider in a single 3D digital core model porosity from different scales (micro and sub-micro).

To build a multiclass model of a core sample, we performed double X-ray μ CT scanning. Before scanning, the sample was seated in the coreholder. The first scan was done for the sample fully saturated with air. Then after air evacuation, we saturated the sample in coreholder with Xenon (Xe) gas. Xe is a non-reactive and highly mobile gas that also has a lower radiolucency than grains. Comparison of two registered and calibrated 3D μ CT data allows to map the distribution of Xe molecules and their amount in the volume of the digital core model. Assuming linear dependence between Xe intensity on the μ CT data difference (μ CT in air - μ CT in Xe) and porosity of the 3D model voxels, it was possible to create a multiclass model. A specific porosity value characterized each model class with a discreteness level equal to 1%. Multiclass model creation includes a few steps:

- Data acquisition for the same sample position, the same resolution and the same X-ray parameters (electrical voltage and current, distance between X-ray source and sample centre, detector exposition and step of sample rotation).
- Image preprocessing (denoising, artefact removing).
- Registration of 3D images (matching images in space) .
- Intensity equilibration (to be sure that minerals without Xe have the same intensity on both 3D images).
- 3D images subtraction (to map only Xe distribution in model volume).
- Parametrization of dependence between Xe intensity and submicron porosity assuming that on subtracted. images, minimum (zero) intensity corresponds to 0% porosity (solid) and maximum intensity corresponds to 100% porosity (big pores).
- Applying determined “intensity-porosity” correlation to all 3D datasets of subtracted images.

It is also possible to construct a multiclass model by combining information about pore space structure from various sources of data: μ CT, scanning microscopy (SEM), and focused ion beam with scanning microscopy (FIB-SEM). One can train a deep neural network to obtain a porosity map directly from SEM or FIB-SEM images. Another opportunity is to create a multiclass model by coarsening a high-resolution binary model to reduce the size of a computational domain but remain the same physical scale of the model.

4.2 Sample classification.

A preprocessor is implemented as a separate module in C++ language; it relies on the Disjoint Set Union data structure [11]. First of all, as it is usual in DRP, it identifies isolated fluid (pure fluid or/and porous) subdomains and removes them. Next, the image is classified. The existence of percolation patch(es) in the computational domain $\Omega^h = \Omega_p^h \cup \Omega_f^h$ is checked. If percolation exists, the Stokes-Brinkman problem (4) is well-posed in the computational domain Ω_h , and the image is classified as an image of Category A. Furthermore, the connectivity of the pure fluid region Ω_f^h is checked. If percolation exists, the image is moved from Category A to Category B, images with Stokes connectivity. Note that after such a preprocessing, Category A contains images that do not have Stokes connectivity but have Stokes-Brinkman connectivity via sequences of pure fluid and porous voxels.

5 Computational experiments.

5.1 Design of computational experiments.

Computational experiments have to be performed for the following purposes:

(i) The accuracy of the developed solvers has to be validated in comparison with data from the literature or in comparison with simulations performed with validated solvers. 3D CT images and generated geometries can be used here.

(ii) The impact of the stopping criteria, the usage of different boundary conditions, and robustness with respect to the problem size have to be studied.

(iii) The main parts of the computer simulations have to be carried out to evaluate the performance of the developed customized solvers for pore-scale simulation on 3D CT images of tight sandstones in the case of unresolved porosity, what is the main goal of this paper.

5.2 Stokes solver. Validation and performance studies on binary images.

Validation on periodic array of impermeable spheres. The developed Stokes solver, SCoPeS-S, is validated first on the classic example of flow around periodic arrangements of solid spheres. Imposing periodic boundary conditions in all three directions, one can consider only a single sphere. The computed permeability is compared with numerical and analytical results from [20] and [39]. An exemplary computation is visualized on Figure 1a. The results are summarized in Table 1. The simulation results show that SCoPeS-S correctly computes the permeability. Also, convergence with respect to the grid size is clearly observed.

Validation on low porosity 3D CT images from the literature. Further, validation of SCoPeS-S is done on five low porosity images listed in Table 2. The computed permeabilities are in good agreement with the data from the literature. The permeabilities computed with the software tools GeoDict, DiMP, and DHD are taken from [34]. It can be seen that the values computed with the newly developed solver, SCoPeS-S, are in the same range as the data from the literature.

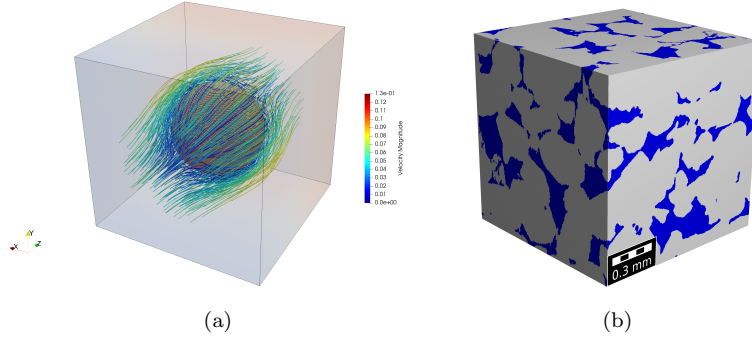


Fig. 1: (a) Velocity magnitude streamlines for periodic arrangements of spheres, diameter $D = 0.5$, resolution $N = 160$. (b) Binary image of size 300^3 with moderate-low porosity $\Phi = 0.21$, colors: grey - solid region, blue - free pores (GeoDict visualization).

D	N=40	N=80	N=160	J&T (ref [20])	S&A (ref [20], [39])
0.1	$9.74 \cdot 10^{-1}$	$9.01 \cdot 10^{-1}$	$9.02 \cdot 10^{-1}$	$9.15 \cdot 10^{-1}$	$9.11 \cdot 10^{-1}$
0.2	$3.77 \cdot 10^{-1}$	$3.78 \cdot 10^{-1}$	$3.80 \cdot 10^{-1}$	$3.84 \cdot 10^{-1}$	$3.82 \cdot 10^{-1}$
0.4	$1.21 \cdot 10^{-1}$	$1.22 \cdot 10^{-1}$	$1.23 \cdot 10^{-1}$	$1.25 \cdot 10^{-1}$	$1.23 \cdot 10^{-1}$
0.6	$4.44 \cdot 10^{-2}$	$4.43 \cdot 10^{-2}$	$4.43 \cdot 10^{-2}$	$4.58 \cdot 10^{-2}$	$4.45 \cdot 10^{-2}$
0.8	$1.29 \cdot 10^{-2}$	$1.31 \cdot 10^{-2}$	$1.31 \cdot 10^{-2}$	$1.38 \cdot 10^{-2}$	$1.32 \cdot 10^{-2}$
1.0	$2.48 \cdot 10^{-3}$	$2.51 \cdot 10^{-3}$	$2.51 \cdot 10^{-3}$	$2.67 \cdot 10^{-3}$	$2.52 \cdot 10^{-3}$

Table 1: Dimensionless permeability \hat{k}_{zz}^{eff} for periodic array of impermeable spheres. D and N denote the diameter of the spheres (with respect to the unit length of the cube) and the number of voxels in one direction, respectively. Relative tolerance $rtol_S = 10^{-3}$ was used in SCoPeS-S.

	Porosity, Φ	GeoDict	SCoPeS-S	DHD	DiMP
A	0.058	$7.1 \cdot 10^{-4}$	$6.5 \cdot 10^{-4}$	$6.7 \cdot 10^{-4}$	$8.4 \cdot 10^{-4}$
B	0.044	$8.8 \cdot 10^{-4}$	$8.1 \cdot 10^{-4}$	$1.0 \cdot 10^{-3}$	$8.7 \cdot 10^{-4}$
C	0.053	$3.9 \cdot 10^{-4}$	$3.1 \cdot 10^{-4}$	$3.2 \cdot 10^{-4}$	$6.6 \cdot 10^{-4}$
D	0.097	$1.18 \cdot 10^{-2}$	$9.83 \cdot 10^{-3}$	$1.02 \cdot 10^{-2}$	$9.38 \cdot 10^{-3}$
E	0.064	$8.3 \cdot 10^{-4}$	$7.3 \cdot 10^{-4}$	$6.8 \cdot 10^{-4}$	$1.26 \cdot 10^{-3}$

Table 2: Validation of SCoPeS-S on five low porosity binary images from [34]. Permeability k_{zz}^{eff} in $mkDa$, $L = 0.00072$ m, relative tolerance $rtol_S = 10^{-5}$.

Validation on 3D CT rock image with low-moderate porosity. In order to further validate the Stokes solver, SCoPeS-S, cross validation with the Stokes solvers from GeoDict for binary 300^3 image with porosity $\Phi = 0.21$ was performed. The results are summarized in Table 3. It can be seen that SCoPeS-S provides results that are within the range of the computations done with GeoDict. For each particular set of the computations, it was decided to gradually decrease the tolerance until the third digit in the computed permeability value is established.

$rtol_S$	SCoPeS	GeoDict			
	SCoPeS-S Pin/Pout	Tol	SimpleFFT Vin/Pout	SimpleFFT Periodic	LIR Periodic
10^{-2}	$6.74 \cdot 10^6$ (491)	10^{-2}	$6.84 \cdot 10^6$ (3928)	$6.37 \cdot 10^6$ (1460)	$6.43 \cdot 10^6$ (325)
10^{-3}	$6.45 \cdot 10^6$ (708)	10^{-3}	$6.88 \cdot 10^6$ (6507)	$6.38 \cdot 10^6$ (2583)	$6.42 \cdot 10^6$ (771)
10^{-4}	$6.46 \cdot 10^6$ (949)	10^{-4}	$6.88 \cdot 10^6$ (7510)	$6.39 \cdot 10^6$ (3102)	$6.42 \cdot 10^6$ (1330)

Table 3: SCoPeS-S and GeoDict (LIR, SimpleFFT) results for binary sample of size 300^3 (Fig. 1b). Permeability k_{zz}^{eff} in $mkDa$ (CPU time in s). SCoPeS-S BC: pressure drop 1 Pa, $L = 0.0011991$ m.

The efficiency of the SCoPeS Stokes solver is comparable to the LIR solver from GeoDict [28] but outperforms the solver SIMPLE-FFT [48].

5.3 Stokes-Brinkman and Darcy solvers. Validation and performance studies on ternary and multiclass images from tight reservoir rocks.

In this Section, the main simulation results are presented. The performance of the developed Stokes-Brinkman solver is systematically investigated for samples coming from tight reservoirs. The performance of SCoPeS-SB and GeoDict Stokes-Brinkman solvers is compared for the considered class of problems. Further on, as discussed above, just Darcy’s problem is solved for images with no Stokes connectivity using SCoPeS-D solver.

5.3.1 Preliminaries: Goals and samples.

We start from three different multiclass samples of size 300^3 , named $S1, S2, S3$, which are sub-samples of a large multiclass sample. Samples $S1, S2, S3$ have 3.79, 3.25, 3.78 mln. non-solid voxels, correspondingly. Recall that *ternary images* are the images composed of solid voxels, fluid voxels, and identical porous voxels, the latter being responsible for all unresolved porosity. Stokes-Brinkman equations have to be solved to compute the permeability for ternary images. For each of these three multiclass samples, the following procedure for increasing porosity and segmenting into ternary images is applied. First, given a threshold $T \in (0, 100]$, we replace all porous voxels $\omega_{i,j,k} \in \Omega_p^h$ having porosity $\phi_{i,j,k} \geq T$ by pure fluid voxels. Next, the remaining porosity is arithmetically averaged with resulting value $\tilde{\phi} \in (0, 100)$. In this way, nine ternary samples are created, which are encoded by N-T- $\tilde{\phi}$.raw, where N=S1,S2,S3, T = 100,90,80, and $\tilde{\phi}$ is resulting averaged porosity. Note, $T = 100$ corresponds to the case when the porosity is just averaged. Finally, constant permeability value is calculated for the averaged porosity $\tilde{\phi}$ according to (17) and assigned to all remaining porous voxels. Table 4 summarizes the connectivity for each of the nine samples. Six of them are from Category A, and three of them are from Category B (marked in **bold**).

The following correlation formula between porosity $\phi_{i,j,k} \in (0, 100)$ and permeability $K_{i,j,k}$ [mkDa] was used:

$$K_{i,j,k} = 7.251 \cdot 10^{-2} \exp(0.147076689 \cdot \phi_{i,j,k}). \quad (17)$$

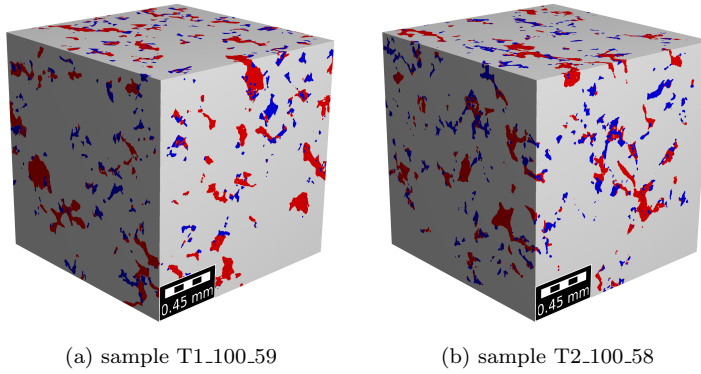


Fig. 2: Ternary samples T1_100_59 and T2_100_58. Colors: grey - solid region, red - unresolved porosity region, blue - free pores. GeoDict visualization.

This correlation formula (17) was derived using empirical petrophysical correlation from FIB-SEM data analysis [3].

Samples	Φ (Res, Unres)	Stokes Connectivity	Stokes-Brinkman Connectivity	File name
S1_100_61	0.14 (0.044, 0.096)	No	Yes	S1_100_61.raw
S1_90_56	0.14 (0.057, 0.083)	No	Yes	S1_90_56.raw
S1_80_50	0.14 (0.070, 0.070)	No	Yes	S1_80_50.raw
S2_100_60	0.14 (0.050, 0.090)	No	Yes	S2_100_60.raw
S2_90_55	0.14 (0.062, 0.078)	Yes	Yes	S2_90_55.raw
S2_80_49	0.14 (0.075, 0.065)	Yes	Yes	S2_80_49.raw
S3_100_58	0.12 (0.050, 0.070)	No	Yes	S3_100_58.raw
S3_90_53	0.12 (0.057, 0.063)	No	Yes	S3_90_53.raw
S3_80_48	0.12 (0.066, 0.054)	Yes	Yes	S3_80_48.raw

Table 4: Porosity and Connectivity of samples

The same segmentation procedure was also applied for two multiclass images of size 600^3 , named $T1, T2$, and having 30.5, 30.7 mln. non-solid voxels, respectively. Additionally, one large multiclass sample, $U1$, of size 1350^3 with 350.8 mln. non-solid voxels was studied. Porosities and connectivities of these samples are summarized in Table A.5.

This collection of images gives us a possibility to perform detailed testing of the performance of the Stokes-Brinkman solver for images with different porosity and different fraction of unresolved regions. The effective permeabilities computed with SCoPeS-SB solver is compared to the results obtained with GeoDict.

Figure 2 presents explanatory pore-space visualization for two ternary samples: $T1_{100.59}$ and $T2_{100.58}$. Also, the result of Stokes-Brinkman simulation on ternary sample $S2_{80.49}$ is shown on Figure 3.

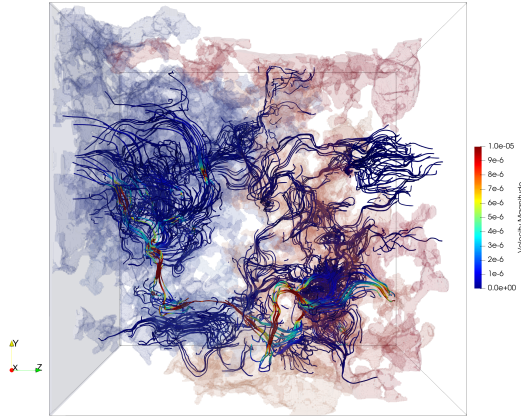


Fig. 3: Velocity magnitude streamlines. Paraview visualization for ternary sample S2_80_49, Stokes-Brinkman problem.

5.3.2 Simulations on ternary images of size 300^3 .

Solving Stokes-Brinkman equations for ternary images of Category A (no Stokes connectivity). Firstly, we consider three Category A images obtained from samples $S2$ and $S3$. The simulation results of comparing the SCoPeS-SB solver and the SimpleFFT solver from GeoDict are presented in Table 5. Also, the simulation results with the LIR solver from GeoDict are shown. However, LIR demonstrated poor performance for low-porosity images, therefore very few results were presented. It can be seen that SimpleFFT and LIR solvers converge very slowly but have the correct tendency, and the computed values are not far from what was expected.

Note, all three images produced from $S1$ sample also belong to Category A, and the corresponding results are available in Table A.1 in the Appendix. In all cases, simulations with SCoPeS-SB show very robust convergence with respect to the selected tolerance. Unlike the GeoDict solvers, the computational time increases moderately when decreasing the tolerance value.

Solving Darcy approximation for ternary images of Category A (no Stokes connectivity). As it was mentioned above, in the case of no Stokes connectivity, it makes sense to first explore approximating Stokes-Brinkman equations with the Darcy equation, and after that solve it to compute the flow, and thus the permeability. The approximation is done by adding artificial permeability in the pure fluid voxels, and after that dropping the viscous terms. Substituting the velocity (in this case with a diagonal matrix) into the continuity equation, we obtain a scalar second order elliptic equation for the pressure.

Simulation results with Darcy model for samples $S2$ and $S3$ are presented in Table 6. The results are computed using Darcy solver SCoPeS-D. For comparison, the effective permeabilities computed with SCoPeS-SB solver are presented in the last line of the Table. One can see that the computations with the Darcy approximation are about 150 times faster compared to SCoPeS-SB, and at the same time the same accuracy in the computation of the permeability of the sample

Sample S2_100_60, Perm of porous voxels 493.0 $mkDa$					
GeoDict				SCoPeS-SB	
Tol	Solver	k_{zz}^{eff} , $mkDa$	CPU, s	$rtol_S$	k_{zz}^{eff} , $mkDa$ (CPU, s)
10^{-1}	SimpleFFT:	$1.20 \cdot 10^2$	20511	10^{-6}	$6.80 \cdot 10^1$ (1564)
$1.2 \cdot 10^{-2}$	SimpleFFT:	$7.95 \cdot 10^1$	172009	10^{-7}	$7.31 \cdot 10^1$ (2769)
$1.9 \cdot 10^{-1}$	LIR:	$1.04 \cdot 10^2$	214560	10^{-8}	$7.27 \cdot 10^1$ (3499)
				10^{-9}	$7.27 \cdot 10^1$ (4090)
Sample S3_100_58, Perm of porous voxels 367.4 $mkDa$					
GeoDict				SCoPeS-SB	
Tol	Solver:	k_{zz}^{eff} , $mkDa$	CPU, s	$rtol_S$	k_{zz}^{eff} , $mkDa$ (CPU, s)
10^{-1}	SimpleFFT:	$4.07 \cdot 10^1$	5862	10^{-7}	$2.23 \cdot 10^1$ (1829)
$1.1 \cdot 10^{-2}$	SimpleFFT:	$2.86 \cdot 10^1$	81435	10^{-8}	$2.54 \cdot 10^1$ (2199)
				10^{-9}	$2.57 \cdot 10^1$ (2693)
				10^{-10}	$2.57 \cdot 10^1$ (3265)
Sample S3_90_53, Perm of porous voxels 176.0 $mkDa$					
GeoDict				SCoPeS-SB	
Tol	Solver:	k_{zz}^{eff} , $mkDa$	CPU, s	$rtol_S$	k_{zz}^{eff} , $mkDa$ (CPU, s)
10^{-1}	SimpleFFT:	$6.52 \cdot 10^1$	10758	10^{-6}	$2.50 \cdot 10^1$ (1487)
$8 \cdot 10^{-2}$	SimpleFFT:	$5.18 \cdot 10^1$	104421	10^{-7}	$5.12 \cdot 10^1$ (1875)
				10^{-8}	$4.92 \cdot 10^1$ (2220)
				10^{-9}	$4.92 \cdot 10^1$ (2733)

Table 5: Ternary samples S2 and S3 of Category A. Permeability k_{zz}^{eff} in $mkDa$ computed with GeoDict (solvers SimpleFFT and LIR with periodic bc), and with SCoPeS-SB with pressure drop bc, $L = 0.0009$ m, nproc=8.

can be achieved. Similar results for samples $S1$ are available in Table A.2 in the Appendix.

Additionally, simulation results from sensitivity study on how the artificial permeability in the Darcy approximation influences the accuracy of the computations are presented in Table A.3 in the Appendix. The sample S1_100_61 is considered there.

K_{Stokes} , $mkDa$	S2_100_60	S3_100_58	S3_90_53
10^5	$4.11 \cdot 10^1$ (42.8)	$2.34 \cdot 10^1$ (43.4)	$3.53 \cdot 10^1$ (42.6)
10^7	$7.43 \cdot 10^1$ (44.1)	$2.57 \cdot 10^1$ (43.1)	$4.95 \cdot 10^1$ (44.2)
10^9	$7.54 \cdot 10^1$ (44.8)	$2.58 \cdot 10^1$ (43.4)	$4.99 \cdot 10^1$ (43.5)
10^{10}	$7.54 \cdot 10^1$ (44.5)	$2.58 \cdot 10^1$ (44.0)	$4.99 \cdot 10^1$ (43.7)
SCoPeS-SB:	$7.27 \cdot 10^1$ (4090)	$2.57 \cdot 10^1$ (3265)	$4.92 \cdot 10^1$ (2733)

Table 6: SCoPeS-D results, Darcy approximation for samples S2_100_60, S3_100_58 and S3_90_53 of Category A. Permeability k_{zz}^{eff} in $mkDa$ (CPU time in s), $rtol_S = 10^{-9}$, $L = 0.0009$ m, nproc=8. BC: pressure drop 1 Pa. The last line for comparison recalls permeability and CPU time when solving Stokes-Brinkman equations.

Solving Stokes-Brinkman equations for ternary images of Category B (Stokes connectivity). Let us now discuss the simulation results for samples from Category B (Stokes connectivity). Consider remaining images obtained from

samples $S2$ and $S3$. Again, the Stokes-Brinkman equations are solved for them, and the computed effective permeability and the CPU time are reported in Table 7. One can observe that for these low porosity samples, SCoPeS-SB demonstrates very good performance. The computed effective permeability values are close to those computed with GeoDict. The convergence with respect to decreasing the tolerance is pronounced and stable. The increasing of the computational time when decreasing the tolerance is very moderate.

Sample S2_90.55, Perm of porous voxels 236.3 mkDa					
GeoDict			SCoPeS-SB		
Tol	Solver	$k_{zz}^{eff}, mkDa$	(CPU, s)	$rtol_S$	$k_{zz}^{eff}, mkDa$ (CPU, s)
10^{-1}	SimpleFFT:	$6.40 \cdot 10^2$	13996	10^{-5}	$5.26 \cdot 10^2$ (1853)
$1.1 \cdot 10^{-2}$	SimpleFFT:	$5.95 \cdot 10^2$	227036	10^{-6}	$5.93 \cdot 10^2$ (2343)
				10^{-8}	$5.91 \cdot 10^2$ (3520)
				10^{-9}	$5.91 \cdot 10^2$ (4243)
Sample S2_80.49, Perm of porous voxels 97.8 mkDa					
GeoDict			SCoPeS-SB		
Tol	Solver:	$k_{zz}^{eff}, mkDa$	(CPU, s)	$rtol_S$	$k_{zz}^{eff}, mkDa$ (CPU, s)
10^{-1}	SimpleFFT:	$6.13 \cdot 10^3$	2103	10^{-5}	$5.95 \cdot 10^3$ (1456)
10^{-2}	SimpleFFT:	$5.88 \cdot 10^3$	7347	10^{-6}	$5.81 \cdot 10^3$ (1816)
10^{-3}	SimpleFFT:	$5.84 \cdot 10^3$	35744	10^{-7}	$5.83 \cdot 10^3$ (2319)
10^{-1}	LIR:	$6.07 \cdot 10^3$	10509	10^{-8}	$5.83 \cdot 10^3$ (2892)
10^{-2}	LIR:	$5.86 \cdot 10^3$	33216		
10^{-3}	LIR:	$5.81 \cdot 10^3$	241828		
Sample S3_80.48, Perm of porous voxels 84.4 mkDa					
GeoDict			SCoPeS-SB		
Tol	Solver:	$k_{zz}^{eff}, mkDa$	(CPU, s)	$rtol_S$	$k_{zz}^{eff}, mkDa$ (CPU, s)
10^{-1}	SimpleFFT:	$1.89 \cdot 10^4$	568	10^{-3}	$1.63 \cdot 10^4$ (703)
10^{-2}	SimpleFFT:	$1.56 \cdot 10^4$	5912	10^{-4}	$1.60 \cdot 10^4$ (955)
10^{-3}	SimpleFFT:	$1.55 \cdot 10^4$	14099	10^{-5}	$1.55 \cdot 10^4$ (1190)
				10^{-7}	$1.55 \cdot 10^4$ (1945)

Table 7: Ternary samples S2 and S3 of Category B. Permeability k_{zz}^{eff} in $mkDa$ computed with GeoDict (solvers SimpleFFT and LIR with periodic bc), and with SCoPeS-SB with pressure drop bc, $L = 0.0009$ m, nproc=8.

Solving Darcy approximation for ternary images of Category B (Stokes connectivity). For comparison, the Darcy approximation is also used for computing the effective permeability of samples from Category B. The results are summarized in Table 8. As expected, the Darcy approximation is not applicable for computing the effective permeability of the considered samples, namely samples for which Stokes connectivity exists. This illustrates the importance of the image classification stage in the presented workflow.

5.3.3 Simulations on multiclass image of size 300^3 .

The developed solver is able to work directly on multiclass images, such that they have individual permeability values in each unresolved voxel. On the one hand, this imposes higher memory requirements to the solver, on the other hand, this

$K_{Stokes}, mkDa$	S2_90.55	S2_80.49	S3_80.48
10^5	$6.13 \cdot 10^1$ (43.3)	$8.19 \cdot 10^1$ (45.0)	$1.39 \cdot 10^2$ (42.5)
10^7	$1.56 \cdot 10^3$ (43.4)	$5.61 \cdot 10^3$ (43.1)	$1.05 \cdot 10^4$ (42.7)
10^9	$1.45 \cdot 10^5$ (43.6)	$5.57 \cdot 10^5$ (42.9)	$1.05 \cdot 10^6$ (43.4)
10^{11}	$1.45 \cdot 10^7$ (44.5)	$5.57 \cdot 10^7$ (43.6)	$1.05 \cdot 10^8$ (43.4)
SCoPeS-SB:	$5.91 \cdot 10^2$ (4243)	$5.83 \cdot 10^3$ (3600)	$1.55 \cdot 10^4$ (1945)

Table 8: SCoPeS-D results, Darcy approximation for samples S2_90.55, S2_80.49 and S3_80.48 of Category B. Permeability k_{zz}^{eff} in $mkDa$ (CPU time in s), $rtol_S = 10^{-9}$, $L = 0.0009$ m, nproc=8. BC: pressure drop 1 Pa. The last line for comparison recalls permeability and CPU time when solving Stokes-Brinkman equations.

feature of the solver might be essential for certain classes of rocks. To illustrate this option, simulations are performed with image $S2$, as a multiclass image having 100 classes of porosity to account for the sub-micron scale effects. The results are summarized in Table 9. Robust convergence of the simulations with respect to the tolerance in the case of multiclass image can be observed. The effective permeabilities computed on the three ternary images produced from the multiclass image $S2$ are also provided in the table. It can be seen that in this particular case the effective permeabilities computed on the multiclass and on the three different ternary images differ significantly. This means that results obtained from simulations on ternary images might not be a good approximation of the results obtained on the true, multiclass grey image, at least if a simple averaging is used when producing ternary image out of a multiclass image.

$rtol_S$	$k_{zz}^{eff}, mkDa$	CPU time, s
10^{-5}	$8.63 \cdot 10^2$	1421
10^{-6}	$5.32 \cdot 10^2$	1883
10^{-7}	$5.29 \cdot 10^2$	2564
10^{-8}	$5.28 \cdot 10^2$	3444
10^{-9}	$5.28 \cdot 10^2$	4285
S2_100.60, 10^{-8}	$7.27 \cdot 10^1$	3499
S2_90.55, 10^{-8}	$5.91 \cdot 10^2$	3520
S2_80.49, 10^{-7}	$5.83 \cdot 10^3$	2319

Table 9: SCoPeS-SB results, permeability k_{zz}^{eff} in $mkDa$ for multiclass sample S2, $L = 0.0009$ m, nproc = 8. BC: pressure drop 1 Pa. Permeabilities of the corresponding ternary samples are also reminded.

5.3.4 Simulations on ternary images of size 600^3 and 1350^3 .

The simulations with larger images show the same behaviour as those with 300^3 images. The simulation results for these images are presented in the Appendix. The classification of the 600^3 with respect to flow connectivity is presented in A.5 The simulation results for images $T1, T2$ of size 600^3 are summarized in Table A.6 for Category A and in Table A.6 for Category B. Similarly to the simulation results

for samples of size 300^3 , one can observe a robust convergence of the SCoPeS-SB solver with respect to the tolerance decrease. It also can be observed that the computational time is still relatively low, especially compared to GeoDict SimpleFFT solver. GeoDict-LIR solver is not explored here, we expect similar performance as for 300^3 images. Comparing computational times reported, e.g., in Tables A.6 and A.1, one can see that the computational time has increased about six times, what is very good result, having in mind the increase of the size of the samples. In general, when using AMG preconditioner, one can expect the computation time to increase proportionally to the number of unknowns. Thus, eight times increase of the CPU time was expected here. The fact that the increase is only six times can be explained by the fact that the more computationally intensive task exhibits better parallel scalability. Simulations with Darcy approximation of Stokes-Brinkman model in the case of 600^3 images show similar performance as in the case of 300^3 images. Results of Darcy simulations are collected in Table A.7 for Category A and in Table A.9 for Category B.

Similarly, the results for *U1* sample of size 1350^3 (Category A) are summarized in Table A.10 for the Stokes-Brinkman problem and in Table A.11 for the Darcy problem.

5.4 Summary.

A workflow containing image classification stage and customized efficient solvers for simulations on 3D CT images of samples from tight reservoirs with multiscale porosity is developed and intensively tested. The proposed stage for classifying images with respect to the existence of Stokes percolation patches allows for selecting the proper solver for each image. The developed solvers are validated using data from the literature and compared with a commercial software tool. Extensive testing on samples from a real tight reservoir are performed. The presented Stokes-Brinkman solver shows very robust convergence and high efficiency. This solver enables simulations not only on ternary, but also on multiclass images. The latter are directly extracted from grey images, and have individual permeability in each porous voxel. It was shown that in the case of missing pure fluid percolation, the Darcy approximation of the Stokes-Brinkman problem can be solved. This gives 10-15 times acceleration of the computations preserving the accuracy.

References

1. Andrä, H., Combaret, N., Dvorkin, J., Glatt, E., Han, J., Kabel, M., Keehm, Y., Krzikalla, F., Lee, M., Madonna, C., et al.: Digital rock physics benchmarks—part ii: Computing effective properties. *Computers & Geosciences* **50**, 33–43 (2013)
2. Arbogast, T., Lehr, H.L.: Homogenization of a darcy–stokes system modeling vuggy porous media. *Computational Geosciences* **10**(3), 291–302 (2006)
3. Avdonin, A., Ebadi, M., Krutko, V.: Application of high-contrast μct and fib-sem for the improvement in the permeability prediction of tight rock samples. In: SPE Russian Petroleum Technology Conference. OnePetro (2021)
4. Balashov, V., Savenkov, E., Chetverushkin, B.: Dimp-hydro solver for direct numerical simulation of fluid microflows within pore space of core samples. *Mathematical Models and Computer Simulations* **12**(2), 110–124 (2020)

5. Balay, S., Abhyankar, S., Adams, M.F., Benson, S., Brown, J., Brune, P., Buschelman, K., Constantinescu, E., Dalcin, L., Dener, A., Eijkhout, V., Gropp, W.D., Hapla, V., Isaac, T., Jolivet, P., Karpeev, D., Kaushik, D., Knepley, M.G., Kong, F., Kruger, S., May, D.A., McInnes, L.C., Mills, R.T., Mitchell, L., Munson, T., Roman, J.E., Rupp, K., Sanan, P., Sarich, J., Smith, B.F., Zampini, S., Zhang, H., Zhang, H., Zhang, J.: PETSc/TAO users manual. Tech. Rep. ANL-21/39 - Revision 3.16, Argonne National Laboratory (2021)
6. Balay, S., Abhyankar, S., Adams, M.F., Brown, J., Brune, P., Buschelman, K., Dalcin, L., Dener, A., Eijkhout, V., Gropp, W.D., Karpeev, D., Kaushik, D., Knepley, M.G., May, D.A., McInnes, L.C., Mills, R.T., Munson, T., Rupp, K., Sanan, P., Smith, B.F., Zampini, S., Zhang, H., Zhang, H.: PETSc Web page. <https://www.mcs.anl.gov/petsc> (2021). URL <https://www.mcs.anl.gov/petsc>
7. Benzi, M., Golub, G.H., Liesen, J.: Numerical solution of saddle point problems. *Acta numerica* **14**, 1–137 (2005)
8. Brinkman, H.C.: A calculation of the viscous force exerted by a flowing fluid on a dense swarm of particles. *Flow, Turbulence and Combustion* **1**(1), 27–34 (1949)
9. Chai, D., Fan, Z., Li, X., et al.: A new unified gas-transport model for gas flow in nanoscale porous media. *SPE Journal* **24**(02), 698–719 (2019)
10. Elman, H.C., Golub, G.H.: Inexact and preconditioned uzawa algorithms for saddle point problems. *SIAM Journal on Numerical Analysis* **31**(6), 1645–1661 (1994)
11. Galler, B.A., Fisher, M.J.: An improved equivalence algorithm. *Communications of the ACM* **7**(5), 301–303 (1964)
12. Golfier, F., Lasseux, D., Quintard, M.: Investigation of the effective permeability of vuggy or fractured porous media from a darcy-brinkman approach. *Computational Geosciences* **19**(1), 63–78 (2015)
13. Griebel, M., Klitz, M.: Homogenization and numerical simulation of flow in geometries with textile microstructures. *Multiscale Modeling & Simulation* **8**(4), 1439–1460 (2010)
14. Guibert, R., Nazarova, M., Horgue, P., Hamon, G., Creux, P., Debenest, G.: Computational permeability determination from pore-scale imaging: sample size, mesh and method sensitivities. *Transport in Porous Media* **107**(3), 641–656 (2015)
15. Harlow, F.H., Welch, J.E.: Numerical calculation of time-dependent viscous incompressible flow of fluid with free surface. *The physics of fluids* **8**(12), 2182–2189 (1965)
16. Iliev, O., Lakdawala, Z., Neßler, K.H., Prill, T., Vutov, Y., Yang, Y., Yao, J.: On the pore-scale modeling and simulation of reactive transport in 3d geometries. *Mathematical Modelling and Analysis* **22**(5), 671–694 (2017). DOI 10.3846/13926292.2017.1356759
17. Iliev, O., Stoyanov, D.: On a flexible tool for upscaling porous media flow problems. *J. Theoret. Appl. Mech* **31**, 18–30 (2001)
18. Javadpour, F., Fisher, D., Unsworth, M., et al.: Nanoscale gas flow in shale gas sediments. *Journal of Canadian Petroleum Technology* **46**(10) (2007)
19. Jia, C., Zheng, M., Zhang, Y.: Some key issues on the unconventional petroleum systems. *Petroleum Research* **1**(2), 113–122 (2016)
20. Jung, Y., Torquato, S.: Fluid permeabilities of triply periodic minimal surfaces. *Physical Review E* **72**(5), 056319 (2005)
21. Karoly, P., Ruehlman, L.S.: Psychological “resilience” and its correlates in chronic pain: findings from a national community sample. *Pain* **123**(1-2), 90–97 (2006)
22. Kelly, S., El-Sobky, H., Torres-Verdín, C., Balhoff, M.T.: Assessing the utility of fib-sem images for shale digital rock physics. *Advances in water resources* **95**, 302–316 (2016)
23. Keyes, D.E., McInnes, L.C., Woodward, C., Gropp, W., Myra, E., Pernice, M., Bell, J., Brown, J., Clo, A., Connors, J., et al.: Multiphysics simulations: Challenges and opportunities. *The International Journal of High Performance Computing Applications* **27**(1), 4–83 (2013)
24. Koroteev, D., Dinariev, O., Evseev, N., Klemin, D., Nadeev, A., Safonov, S., Gurpinar, O., Berg, S., Van Kruijsdijk, C., Armstrong, R., et al.: Direct hydrodynamic simulation of multiphase flow in porous rock. *Petrophysics-The SPWLA Journal of Formation Evaluation and Reservoir Description* **55**(04), 294–303 (2014)
25. Krotkiewski, M., Ligaarden, I.S., Lie, K.A., Schmid, D.W.: On the importance of the stokes-brinkman equations for computing effective permeability in karst reservoirs. *Communications in Computational Physics* **10**(5), 1315–1332 (2011)
26. Li, S., Sang, Q., Dong, M., Luo, P.: Determination of inorganic and organic permeabilities of shale. *International Journal of Coal Geology* **215**, 103296 (2019)
27. Linden, S., Cheng, L., Wiegmann, A.: Specialized methods for direct numerical simulations in porous media. *Math2Market GmbH* (2018)

28. Linden, S., Wiegmann, A., Hagen, H.: The lir space partitioning system applied to the stokes equations. *Graphical Models* **82**, 58–66 (2015)
29. Lu, X., Armstrong, R.T., Mostaghimi, P.: Analysis of gas diffusivity in coal using micro-computed tomography. *Fuel* **261**, 116384 (2020)
30. Marco Discacciati, A.Q.: Navier-stokes/darcy coupling: modeling, analysis, and numerical approximation. *Revista Matemática Complutense* **22**(2), 315–426 (2009). URL <http://eudml.org/doc/43558>
31. Math2Market: Geodict web page. <https://www.geodict.com/Solutions/aboutGD.php>. URL <https://www.geodict.com/Solutions/aboutGD.php>. Accessed: 21-09-26
32. Mostaghimi, P., Blunt, M., Bijeljic, B.: Computations of absolute permeability on micro-ct images. *Mathematical Geosciences* **45** (2012). DOI 10.1007/s11004-012-9431-4
33. OpenFoam: Openfoam web page. <https://www.openfoam.com>. URL <https://www.openfoam.com>. Accessed: 21-11-04
34. Orlov, D., Ebadi, M., Muravleva, E., Volkhonskiy, D., Erofeev, A., Savenkov, E., Balashov, V., Belozherov, B., Krutko, V., Yakimchuk, I., et al.: Different methods of permeability calculation in digital twins of tight sandstones. *Journal of Natural Gas Science and Engineering* **87**, 103750 (2021)
35. Patankar, S.V., Spalding, D.B.: A calculation procedure for heat, mass and momentum transfer in three-dimensional parabolic flows. In: *Numerical prediction of flow, heat transfer, turbulence and combustion*, pp. 54–73. Elsevier (1983)
36. Ruge, J.W., Stüben, K.: Algebraic multigrid. In: *Multigrid methods*, pp. 73–130. SIAM (1987)
37. Saad, Y.: *Iterative methods for sparse linear systems*. SIAM (2003)
38. Sander, R., Pan, Z., Connell, L.D.: Laboratory measurement of low permeability unconventional gas reservoir rocks: A review of experimental methods. *Journal of Natural Gas Science and Engineering* **37**, 248–279 (2017)
39. Sangani, A.S., Acrivos, A.: Slow flow through a periodic array of spheres. *International Journal of Multiphase Flow* **8**(4), 343–360 (1982)
40. Saxena, N., Hofmann, R., Alpak, F.O., Berg, S., Dietderich, J., Agarwal, U., Tandon, K., Hunter, S., Freeman, J., Wilson, O.B.: References and benchmarks for pore-scale flow simulated using micro-ct images of porous media and digital rocks. *Advances in Water Resources* **109**, 211–235 (2017)
41. Thermofisher: Thermofisher web page. <https://www.thermofisher.com>. URL <https://www.thermofisher.com>. Accessed: 21-11-04
42. Turek, S.: *Efficient Solvers for Incompressible Flow Problems: An Algorithmic and Computational Approaches*, vol. 6. Springer Science & Business Media (1999)
43. Ulrich, H.: *Homogenization and Porous Mediae*. Springer-Verlag New York (1997)
44. Verfurth, R.: A combined conjugate gradient-multi-grid algorithm for the numerical solution of the stokes problem. *IMA Journal of Numerical Analysis* **4**(4), 441–455 (1984)
45. Verri, I., Della Torre, A., Montenegro, G., Onorati, A., Duca, S., Mora, C., Radaelli, F., Trombin, G.: Development of a digital rock physics workflow for the analysis of sandstones and tight rocks. *Journal of Petroleum Science and Engineering* **156**, 790–800 (2017)
46. Wang, W., Fan, D., Sheng, G., Chen, Z., Su, Y.: A review of analytical and semi-analytical fluid flow models for ultra-tight hydrocarbon reservoirs. *Fuel* **256**, 115737 (2019)
47. Whitaker, S.: Flow in porous media i: A theoretical derivation of darcy’s law. *Transport in porous media* **1**(1), 3–25 (1986)
48. Wiegmann, A.: Computation of the permeability of porous materials from their microstructure by fff-stokes. *Berichte des Fraunhofer ITWM*, 2007 (129) (2007)
49. Willian J. Layton Schieweck Friedhelm, I.Y.: Coupling fluid flow with porous media flow. *SIAM Journal on Numerical Analysis* **40**(6), 2195–2218 (2003)
50. Yang, U.M., et al.: Boomeramg: a parallel algebraic multigrid solver and preconditioner. *Applied Numerical Mathematics* **41**(1), 155–177 (2002)

Appendix

This Appendix summarizes some further simulation results.

A Simulations on S1 ternary images of size 300^3 .

All three samples produced from the S1 image belong to category A, no Stokes connectivity. Thus it is expected that the results in this case will be similar to those for S2_100_60, S2_90_55 and S3_90_53, which also belong to category A. Indeed, the results from Table A.1 below are similar to those from Table 4 from the main text.

Sample S1_100_61, Perm of porous voxels 571.2 mkDa					
GeoDict			SCoPeS-SB		
Tol	Solver	$k_{zz}^{eff}, mkDa$	CPU, s	$rtol_S$	$k_{zz}^{eff}, mkDa$ (CPU, s)
10^{-1}	SimpleFFT:	$8.74 \cdot 10^1$	4471	10^{-6}	$3.42 \cdot 10^1$ (1210)
10^{-2}	SimpleFFT:	$6.16 \cdot 10^1$	61406	10^{-7}	$5.69 \cdot 10^1$ (1522)
10^{-1}	LIR	$1.24 \cdot 10^2$	33968	10^{-8}	$5.68 \cdot 10^1$ (1898)
$9.95 \cdot 10^{-2}$	LIR	$6.46 \cdot 10^1$	459561	10^{-9}	$5.68 \cdot 10^1$ (2390)
Sample S1_90_56, Perm of porous voxels 273.8 mkDa					
GeoDict			SCoPeS-SB		
Tol	Solver:	$k_{zz}^{eff}, mkDa$	CPU, s	$rtol_S$	$k_{zz}^{eff}, mkDa$ (CPU, s)
10^{-1}	SimpleFFT:	$1.17 \cdot 10^2$	5357	10^{-6}	$5.82 \cdot 10^1$ (1227)
$2 \cdot 10^{-2}$	SimpleFFT:	$7.11 \cdot 10^1$	70690	10^{-7}	$6.45 \cdot 10^1$ (1584)
				10^{-8}	$6.34 \cdot 10^1$ (1942)
				10^{-9}	$6.33 \cdot 10^1$ (2431)
Sample S1_80_50, Perm of porous voxels 113.3 mkDa					
GeoDict			SCoPeS-SB		
Tol	Solver:	$k_{zz}^{eff}, mkDa$	CPU, s	$rtol_S$	$k_{zz}^{eff}, mkDa$ (CPU, s)
10^{-1}	SimpleFFT:	$8.07 \cdot 10^1$	16532	10^{-6}	$6.42 \cdot 10^1$ (1292)
$5 \cdot 10^{-3}$	SimpleFFT:	$6.51 \cdot 10^1$	228113	10^{-7}	$6.03 \cdot 10^1$ (1628)
				10^{-8}	$7.01 \cdot 10^1$ (1991)
				10^{-9}	$6.00 \cdot 10^1$ (2393)

Table A.1: Ternary samples S1 of Category A. Permeability k_{zz}^{eff} in $mkDa$ computed with GeoDict (solvers SimpleFFT and LIR with periodic bc) and with SCoPeS-SB with pressure drop bc, $L = 0.0009$ m, nproc=8.

As mentioned above, all three samples produced from the S1 image belong to Category A. Thus, it is expected that the accuracy and the performance of the Darcy approximation in this case will be similar to those for S2_100_60, S2_90_55, and S3_90_53, which also belong to category A. Indeed, the results from Table A.2 below are similar to those from Table 6 from the main text.

$K_{Stokes}, mkDa$	S1_100.61	S1_90.56	S1_80.50
10^5	$4.54 \cdot 10^1$ (43.2)	$4.48 \cdot 10^1$ (43.5)	$4.07 \cdot 10^1$ (42.6)
10^7	$5.70 \cdot 10^1$ (43.6)	$6.35 \cdot 10^1$ (43.6)	$6.01 \cdot 10^1$ (43.3)
10^9	$5.72 \cdot 10^1$ (44.1)	$6.39 \cdot 10^1$ (44.1)	$6.04 \cdot 10^1$ (43.6)
10^{10}	$5.72 \cdot 10^1$ (44.5)	$6.39 \cdot 10^1$ (43.7)	$6.04 \cdot 10^1$ (43.1)
SCoPeS-SB:	$5.68 \cdot 10^1$ (2390)	$6.34 \cdot 10^1$ (2431)	$6.00 \cdot 10^1$ (2393)

Table A.2: SCoPeS-D results, Darcy approximation for samples S1_100.61, S1_90.56 and S1_80.50 of Category A. Permeability k_{zz}^{eff} in $mkDa$ (CPU time in s), $rtol_S = 10^{-9}$, $L = 0.0009$ m, nproc=8. BC: pressure drop 1 Pa. The last line for comparison recalls permeability and CPU time when solving Stokes-Brinkman equations.

B Darcy approximation, sensitivity study

As mentioned, Darcy approximation of Stokes-Brinkman equations is used for images of Category A. Its accuracy and performance were examined before its further usage. Simulation results from sensitivity study on how the artificial permeability in the Darcy approximation influences the accuracy of the computations are presented in Table A.3 in the Appendix. The sample S1_100.61 is considered here. This Table contains three subtables. In the first one, the fictitious permeability K_{Stokes} in the Stokes (pure fluid) voxels is fixed to a moderate value $10^{-6} m^2$, and the tolerance for the iterative method is varied. In the second subtable, a relatively rough tolerance is fixed for the iterative method (10^{-4}) and the fictitious permeability K_{Stokes} is varied. Finally, in the third subtable, the tolerance 10^{-9} is fixed for the iterative method, and the fictitious permeability is varied. Comparing to the results from Table A.3, one can see that Darcy approximation can be successfully used for fast and accurate computation of the effective permeability of samples in the case of no Stokes connectivity. The results from Table A.3 show that relatively low value for the fictitious permeability should be set in the Stokes voxels, and the iterative method should be converged with high accuracy. The latter however, in this particular case does not influence essentially the computational time.

$rtol_S$	$K_{Stokes}, mkDa$	$k_{zz}^{eff}, mkDa$	CPU time, s
10^{-4}	10^6	$5.51 \cdot 10^1$	39.2
10^{-5}	10^6	$5.51 \cdot 10^1$	40.2
10^{-6}	10^6	$5.51 \cdot 10^1$	40.6
10^{-4}	10^6	$5.51 \cdot 10^1$	39.2
10^{-4}	10^8	$5.75 \cdot 10^1$	38.8
10^{-4}	10^{10}	$2.31 \cdot 10^2$	39.3
10^{-9}	10^5	$4.54 \cdot 10^1$	43.2
10^{-9}	10^6	$5.51 \cdot 10^1$	43.4
10^{-9}	10^{11}	$5.72 \cdot 10^1$	44.4

Table A.3: SCoPeS-D results, Darcy approximation for sample S1_100.61; $L = 0.0009$ m, nproc=8. BC: pressure drop 1 Pa.

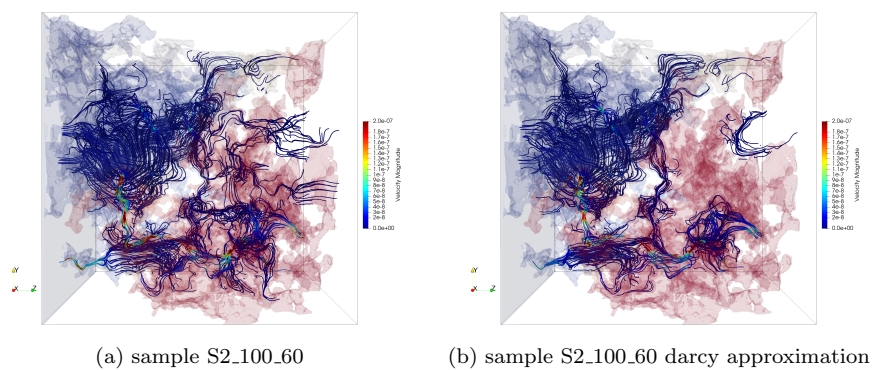


Fig. A.1: sample S2.100.60

C Visual comparison of flow simulations with Stokes-Brinkman system and with its Darcy approximation

It was shown above that Darcy approximation can be efficiently used to compute integral quantities, such as permeability, for samples with no Stokes connectivity. Streamlines from computations with Stokes-Brinkman system and with its Darcy approximation are plotted on Fig. A.1. It can be seen that Darcy approximation not only accurately compute integral quantities, but also handles well the local behaviour of the flow.

D Hardware/Software Specifications

Samples $300^3, 600^3$	
Hardware model	Operating System
2 x Intel Xeon E5-2687W v4@3.00 GHz, RAM 528 Gb DDR4 2400 Hz	Linux 4.15.0-154-generic Ubuntu 18.04.6
Samples 1350^3	
Dell PowerEdge R640, 2 x Intel Xeon Gold 6150@2.7 GHz, RAM 1536 Gb DDR4	CentOS Linux release 7.9.2009

Table A.4: Hardware/Software Specification

E Simulations on ternary images of size 600^3 and 1350^3

Samples	ϕ (Res, Unres)	Stokes Connectivity	Stokes-Brinkman Connectivity	File name
T1_100_59	0.141 (0.051, 0.089)	No	Yes	T1_100_59.raw
T1_90_54	0.141 (0.062, 0.079)	No	Yes	T1_90_54.raw
T1_80_49	0.141 (0.073, 0.067)	Yes	Yes	T1_80_49.raw
T2_100_58	0.142 (0.051, 0.091)	No	Yes	T2_100_58.raw
T2_90_54	0.142 (0.061, 0.081)	No	Yes	T2_90_54.raw
T2_80_49	0.142 (0.072, 0.070)	Yes	Yes	T2_80_49.raw
U1_100_59	0.143 (0.052, 0.091)	No	Yes	U1_100_59.raw

Table A.5: Porosity and Connectivity of the samples

Sample T1_100_59, Perm of porous voxels 425.6 $mkDa$					
GeoDict			SCoPeS-SB		
Tol	Solver	k_{zz}^{eff} , $mkDa$	(CPU, s)	$rtol_S$	k_{zz}^{eff} , $mkDa$ (CPU, s)
$2.2 \cdot 10^{-1}$	SimpleFFT	$6.49 \cdot 10^1$	170969	10^{-6}	$5.61 \cdot 10^1$ (6082)
				10^{-7}	$3.33 \cdot 10^1$ (8148)
				10^{-8}	$3.37 \cdot 10^1$ (10538)
				10^{-9}	$3.38 \cdot 10^1$ (13027)
Sample T1_90_54, Perm of porous voxels 204.0 $mkDa$					
GeoDict			SCoPeS-SB		
Tol	Solver:	k_{zz}^{eff} , $mkDa$	(CPU, s)	$rtol_S$	k_{zz}^{eff} , $mkDa$ (CPU, s)
$7.2 \cdot 10^{-1}$	SimpleFFT:	$1.41 \cdot 10^2$	52369	10^{-6}	$3.38 \cdot 10^1$ (6059)
				10^{-7}	$5.51 \cdot 10^1$ (8035)
				10^{-8}	$5.48 \cdot 10^1$ (10240)
Sample T2_100_58, Perm of porous voxels 367.4 $mkDa$					
GeoDict			SCoPeS-SB		
Tol	Solver:	k_{zz}^{eff}	(CPU, s)	$rtol_S$	k_{zz}^{eff} , $mkDa$ (CPU, s)
$2 \cdot 10^{-1}$	SimpleFFT:	$4.25 \cdot 10^1$	1.2509e+6	10^{-6}	$3.61 \cdot 10^1$ (6191)
				10^{-7}	$3.35 \cdot 10^1$ (8320)
				10^{-8}	$3.36 \cdot 10^1$ (10425)
Sample T2_90_54, Perm of porous voxels 204.0 $mkDa$					
GeoDict			SCoPeS-SB		
Tol	Solver:	k_{zz}^{eff} , $mkDa$	(CPU, s)	$rtol_S$	k_{zz}^{eff} , $mkDa$ (CPU, s)
$2.4 \cdot 10^{-1}$	SimpleFFT:	$9.32 \cdot 10^1$	815269	10^{-6}	$5.94 \cdot 10^1$ (6333)
				10^{-7}	$6.38 \cdot 10^1$ (8371)
				10^{-8}	$6.51 \cdot 10^1$ (10456)
				10^{-9}	$6.51 \cdot 10^1$ (13191)

Table A.6: Ternary samples T1 and T2 with no Stokes connectivity. Permeability k_{zz}^{eff} in $mkDa$ computed with GeoDict (solvers SimpleFFT and LIR with periodic bc) and with SCoPeS-SB with pressure drop bc, $L = 0.0018$ m, nproc=8.

$K_{Stokes},$ $mkDa$	T1_100_59	T1_90_54	T2_100_58	T2_90_54
10^5	$2.58 \cdot 10^1$ (260)	$2.18 \cdot 10^1$ (319)	$2.17 \cdot 10^1$ (321)	$2.36 \cdot 10^1$ (322)
10^7	$3.39 \cdot 10^1$ (255)	$5.84 \cdot 10^1$ (318)	$3.36 \cdot 10^1$ (330)	$7.23 \cdot 10^1$ (327)
10^9	$3.40 \cdot 10^1$ (264)	$6.21 \cdot 10^1$ (325)	$3.39 \cdot 10^1$ (334)	$7.77 \cdot 10^1$ (332)
10^{11}	$3.41 \cdot 10^1$ (269)	$6.22 \cdot 10^1$ (320)	$3.39 \cdot 10^1$ (334)	$7.77 \cdot 10^1$ (331)
SCoPeS-SB:	$3.30 \cdot 10^1$ (9472)	$4.33 \cdot 10^1$ (10425)	$3.36 \cdot 10^1$ (10425)	$6.51 \cdot 10^1$ (10456)

Table A.7: SCoPeS-D results, Darcy approximation for samples T1_100_59, T1_90_54, T2_100_58 and T2_90_54. Permeability k_{zz}^{eff} in $mkDa$ (CPU time in s), $rtol_S = 10^{-9}$, $L = 0.0018$ m, nproc=8. BC: pressure drop 1 Pa. The last line for comparison recalls permeability and CPU time when solving Stokes-Brinkman equations.

Sample T1_80_49, Perm of porous voxels 97.8 $mkDa$					
GeoDict				SCoPeS-SB	
Tol	Solver	$k_{zz}^{eff}, mkDa$	(CPU, s)	$rtol_S$	$k_{zz}^{eff}, mkDa$ (CPU, s)
10^{-1}	SimpleFFT	$6.45 \cdot 10^2$	155062	10^{-5}	$5.68 \cdot 10^2$ (4849)
$1.3 \cdot 10^{-2}$	SimpleFFT	$6.01 \cdot 10^2$	834989	10^{-6}	$6.06 \cdot 10^2$ (6208)
				10^{-7}	$5.88 \cdot 10^2$ (8215)
				10^{-8}	$5.88 \cdot 10^2$ (10460)
Sample T2_80_49, Perm of porous voxels 97.8 $mkDa$					
GeoDict				SCoPeS-SB	
Tol	Solver:	$k_{zz}^{eff}, mkDa$	(CPU, s)	$rtol_S$	$k_{zz}^{eff}, mkDa$ (CPU, s)
10^{-1}	SimpleFFT:	$6.59 \cdot 10^3$	6087	10^{-4}	$1.94 \cdot 10^3$ (4238)
$2.6 \cdot 10^{-2}$	SimpleFFT	$1.59 \cdot 10^3$	682309	10^{-5}	$1.49 \cdot 10^3$ (5352)
				10^{-6}	$1.57 \cdot 10^3$ (6899)
				10^{-7}	$1.57 \cdot 10^3$ (8801)

Table A.8: Ternary samples T1 and T2 of Category B. Permeability k_{zz}^{eff} in $mkDa$ computed with GeoDict (solvers SimpleFFT and LIR with periodic bc) and with SCoPeS-SB with pressure drop bc, $L = 0.0018$ m, nproc=8.

$K_{Stokes}, mkDa$	T1_80_49	T2_80_49
10^5	$2.64 \cdot 10^1$ (314)	$3.45 \cdot 10^1$ (320)
10^7	$1.04 \cdot 10^3$ (320)	$1.65 \cdot 10^3$ (321)
10^9	$1.02 \cdot 10^5$ (325)	$1.60 \cdot 10^5$ (322)
10^{11}	$1.02 \cdot 10^7$ (323)	$1.60 \cdot 10^7$ (327)
SCoPeS-SB:	$5.89 \cdot 10^2$ (8215)	$1.57 \cdot 10^3$ (6899)

Table A.9: SCoPeS-D results, Darcy approximation for samples S2_90_55, S2_80_49 and S3_80_48. Permeability k_{zz}^{eff} in $mkDa$ (CPU time in s), $rtol_S = 10^{-9}$, $L = 0.0018$ m, nproc=8. BC: pressure drop 1 Pa. The last line for comparison recalls permeability and CPU time when solving Stokes-Brinkman equations.

Sample U1_100_59, Perm of porous voxels 425.60 $mkDa$					
GeoDict				SCoPeS-SB	
Tol	Solver	$k_{zz}^{eff}, mkDa$	(CPU, s)	$rtol_S$	$k_{zz}^{eff}, mkDa$ (CPU, s)
$3.92 \cdot 10^{-1}$	SimpleFFT	$9.17 \cdot 10^1$	1.11362e+06	10^{-6}	$3.34 \cdot 10^1$ (99841)
10^{-1} (nproc=16)	SimpleFFT	$6.06 \cdot 10^1$	865126	10^{-7}	$3.29 \cdot 10^1$ (129588)
10^{-1}	LIR	divergence		10^{-8}	$3.28 \cdot 10^1$ (165821)
				10^{-9}	$3.28 \cdot 10^1$ (205090)

Table A.10: Ternary sample U1 with no Stokes connectivity. Permeability k_{zz}^{eff} in $mkDa$ computed with GeoDict (solvers SimpleFFT with periodic bc) and with SCoPeS-SB with pressure drop bc, $L = 0.0027$ m, nproc=8.

$K_{Stokes}^{-1}, mkDa$	U1_100_59
10^5	$2.35 \cdot 10^1$ (7255)
10^7	$3.34 \cdot 10^1$ (7373)
10^9	$3.37 \cdot 10^1$ (7537)
10^{11}	$3.37 \cdot 10^1$ (7437)
SCoPeS-SB	$3.28 \cdot 10^1$ (205090)

Table A.11: SCoPeS-D results, Darcy approximation for sample U1. Permeability k_{zz}^{eff} in $mkDa$ (CPU time in s), $rtol_S = 10^{-9}$, $L = 0.0009$ m, nproc=8. BC: pressure drop 1 Pa. The last line for comparison recalls permeability and CPU time when solving Stokes-Brinkman equations.

sample	# non-solid voxels	SCoPeS-SB (Gb)	SCoPeS-D (Gb)	GeoDict SimpleFFT (Gb)
S1_100_61	3.79 mln.	19.7	13.8	2.2
T1_100_59	30.5 mln.	104.8	87.5	16.5
U1_100_59	350.8 mln.	1025.2	896.3	183.6

Table A.12: Memory (RAM) usage of SCoPeS comparing with GeoDict-SimpleFFT.